

FAST TRACK PAPER

Calculating horizontal stress orientations with full or partial knowledge of the tectonic stress tensor

Björn Lund¹ and John Townend²

¹Department of Earth Sciences, Uppsala University, Villavägen 16, 752 36 Uppsala, Sweden

²Institute of Geophysics, School of Geography, Environment, and Earth Sciences, Victoria University of Wellington, PO Box 600, Wellington, New Zealand

Accepted 2007 April. Received 2007 April 20; in original form 2007 January 23

SUMMARY

Earthquakes potentially serve as abundant and cost-effective gauges of tectonic stress provided that reliable means exist of extracting robust stress parameters. Several algorithms have been developed for this task, each of which typically provides information on the orientations of the three principal stresses and a single stress magnitude parameter. A convenient way of displaying tectonic stress results is to map the azimuth of maximum horizontal compressive stress, which is usually approximated using the azimuth of the larger subhorizontal principal stress. This approximation introduces avoidable errors that depend not only on the principal stress axes' plunges but also on the value of the stress magnitude parameter. Here we outline a method of computing the true direction of maximum horizontal compressive stress (S_H) and show that this computation can be performed using only the four stress parameters obtained in routine focal mechanism stress estimation. Using theoretical examples and new stress inversion results obtained with focal mechanism data from the central Grímsey lineament, northern Iceland, we show that the S_H axis may differ by tens of degrees from its commonly adopted proxy. In order to most appropriately compare tectonic stress estimates with other geophysical parameters, such as seismic fast directions or geodetically measured strain rate tensors, or to investigate spatiotemporal variations in stress, we recommend that full use be made of the routinely estimated stress parameters and that a formal axis of maximum horizontal compression be calculated.

Key words: fault mechanics, focal mechanism, Grímsey lineament, horizontal stress, Iceland, stress tensor.

1 INTRODUCTION

The rapidly increasing geographic scope and density of continuous seismic networks provides a rich data set for local tectonic stress estimates (the 'state of tectonic stress'; see Hardebeck & Michael 2004; Townend & Zoback 2006; Townend 2006, for recent reviews). The state of tectonic stress at any point in the Earth is fully defined by six independent parameters, which are typically represented as either the six components s_{ij} of a 3×3 symmetric matrix S or three angles specifying the orientation of the stress tensor's eigenvectors with respect to geographic coordinates and three corresponding eigenvalues. Whereas borehole measurements enable all six stress tensor parameters to be inferred in ideal circumstances (e.g. Zoback *et al.* 2003), generally only a four-parameter subset of these parameters can be determined in typical geological and seismological contexts. Several algorithms have been developed for this task (e.g. Angelier 1979; Gephart & Forsyth 1984; Lund & Slunga 1999; Abers & Gephart 2001; Arnold & Townend 2007), each of which typically provides information on the orientations of the three principal stresses and a single stress magnitude parameter.

Displaying either full or partial representations of the tectonic stress tensor in a readily interpretable manner is complicated. It is common to use stereographic representations to show individual results and maps to display the axis of maximum horizontal compressive stress, hereafter referred to as S_H (e.g. Balfour *et al.* 2005). Defining a suitable scalar representation of the stress field has also proven useful in recent studies of temporal changes in stress associated with nearby volcanic eruptions or large earthquakes (e.g. Roman *et al.* 2004; Bohnhoff *et al.* 2006, and references therein). Moreover, it is becoming increasingly feasible to interpret seismological estimates of tectonic stress directions in conjunction with dynamic modelling results (Flesch *et al.* 2000; Townend & Zoback 2004), fault slip inversions (Becker *et al.* 2005), crustal anisotropy at borehole and regional scales (Balfour *et al.* 2005; Boness & Zoback 2006a,b), or geodetic estimates of horizontal principal strain rates (Townend & Zoback 2006).

An intuitive method of identifying the direction of maximum horizontal stress is to simply adopt the trend of the larger subhorizontal stress. This approach has been adopted in several of the studies referred to above, but is appropriate only when one of the

three principal stresses is strictly vertical (Lund 2000). For a perfectly Andersonian state of stress with one vertical and two unequal horizontal stresses (Anderson 1951), \mathbf{S}_H is parallel to the axis of maximum principal stress, unless that axis is vertical, in which case it is parallel to the axis of intermediate stress. The Andersonian model of stress, which stems from the inference that the Earth's approximately flat surface supports no shear stresses, accounts rather well for typical stress geometries observed in a variety of tectonic situations (e.g. Townend 2006, and references therein). However, stress estimation from seismological data, in particular, invariably yields results in which none of the principal stress axes is exactly vertical.

In this paper, we show how to estimate the 'true' \mathbf{S}_H orientation (in a mathematical sense) from routine stress inversion results or an arbitrary stress tensor. We do not address the question here of whether departures from the idealized geometries represent observational uncertainties or real ambient conditions, which is the subject of ongoing research. When none of the three principal stresses is strictly vertical, \mathbf{S}_H does *not* simply coincide with the commonly adopted horizontal projection of the larger subhorizontal stress, which we refer to below as the maximum horizontal stress proxy, \mathbf{S}_P . Nevertheless, a true \mathbf{S}_H direction can be straightforwardly computed irrespective of the principal stresses' orientations and with only partial knowledge of the stress tensor. We show the importance of correctly calculating \mathbf{S}_H , especially when spatiotemporal changes in stress are under investigation, by investigating the variation of \mathbf{S}_H with respect to the four seismologically estimable stress parameters. We close by briefly illustrating how \mathbf{S}_H and \mathbf{S}_P compare in a case study using data from the Grimsey lineament in northern Iceland.

2 CALCULATING THE DIRECTION OF MAXIMUM HORIZONTAL STRESS

The analysis below is based on the observation that the direction in which horizontal compressive stress is greatest corresponds to the direction of the normal of the vertical plane experiencing maximum normal stress (Lund 2000). For completeness, we first derive the orientation and magnitude of the maximum horizontal stress when all six stress tensor parameters are known (Section 2.1). We then show how the orientation, but not the magnitude, of the maximum horizontal stress can be found from the four stress tensor components obtained in routine inversion of focal mechanism data (Section 2.2).

Two coordinate systems are of importance here: a principal stress coordinate system, \mathbb{S} , with unit vectors $\{\hat{\mathbf{s}}_1, \hat{\mathbf{s}}_2, \hat{\mathbf{s}}_3\}$ aligned along the eigenvectors whose eigenvalues are $S_1 \geq S_2 \geq S_3$, respectively; and a geographic coordinate system, \mathbb{G} , with unit vectors $\{\hat{\mathbf{g}}_1, \hat{\mathbf{g}}_2, \hat{\mathbf{g}}_3\}$ aligned with the north, east and down directions, respectively.

In this paper, matrices are represented in sans serif upper-case letters (e.g. \mathbf{S}), vectors in bold lower-case letters (e.g. \mathbf{n}), and vector magnitudes in upper-case italics (e.g. $S_n = \|\mathbf{s}_n\|$; Table 1). The components of matrices and vectors are represented, for example, as s_{ij} and n_i , respectively, and a caret and subscript (e.g. $\hat{\mathbf{s}}_i$) are used together to denote the i th unit basis vector of a coordinate system ($i = 1, 2, 3$). Vector orientations are expressed in terms of trend and plunge angles as *trend/plunge* (e.g. 135/25). For convenience, we use upper-case bold symbols for the two most frequently used parameters, namely the vectors of maximum horizontal stress \mathbf{S}_H and its proxy \mathbf{S}_P .

Table 1. Mathematical symbols. Indices i and j each span the range 1, 2, 3, and a caret ($\hat{\cdot}$) denotes a unit vector.

Symbol	Explanation
α	Arbitrary trend angle measured clockwise from north
α_H	Trend of the maximum horizontal compressive stress
α_P	Trend of the maximum horizontal stress proxy
$\mathbf{A}_{\mathbb{X}\mathbb{Y}}$	Rotation matrix between coordinate systems \mathbb{Y} and \mathbb{X}
\mathbf{D}	Deviatoric stress tensor (with respect to $S_3\mathbf{l}$)
\mathbf{d}_n	Deviatoric normal stress vector
D_n	Magnitude of the deviatoric normal stress vector
$\hat{\mathbf{g}}_i$	Axes of the north-east-down coordinate system \mathbb{G}
\mathbf{l}	Identity matrix
$\hat{\mathbf{n}}_{\mathbb{X}}$	Unit normal vector represented in coordinate system \mathbb{X}
n_i	Components of the vector \mathbf{n}
R	Stress ratio equal to $(S_1 - S_2)/(S_1 - S_3)$
\mathbf{S}	Stress tensor
\mathbf{S}_H	Maximum horizontal compressive stress vector
$\hat{\mathbf{s}}_i$	Axes of the principal stress coordinate system \mathbb{S}
s_{ij}	Components of matrix \mathbf{S} (i.e. the j th component of $\hat{\mathbf{s}}_i$)
\mathbf{s}_n	Normal stress vector
S_n	Magnitude of the normal stress vector
\mathbf{S}_P	Maximum horizontal stress proxy vector
S_i	Magnitudes of the principal stresses ($S_1 \geq S_2 \geq S_3$)
\mathbb{X}	Arbitrary coordinate system

2.1 Calculating the direction of maximum horizontal stress using the complete stress tensor

We define a vertical plane in the geographic coordinate system, \mathbb{G} , using its unit normal vector, $\hat{\mathbf{n}}_{\mathbb{G}}^T = (n_N, n_E, n_D) = (\cos \alpha, \sin \alpha, 0)$, where α is the normal's trend angle measured clockwise from north and the plane's strike is $\alpha + \pi/2$. We represent $\hat{\mathbf{n}}$ with respect to the principal stress coordinate system \mathbb{S} using the transformation matrix

$$\mathbf{A}_{\mathbb{S}\mathbb{G}} = \begin{pmatrix} \hat{\mathbf{s}}_1 \cdot \hat{\mathbf{g}}_1 & \hat{\mathbf{s}}_1 \cdot \hat{\mathbf{g}}_2 & \hat{\mathbf{s}}_1 \cdot \hat{\mathbf{g}}_3 \\ \hat{\mathbf{s}}_2 \cdot \hat{\mathbf{g}}_1 & \hat{\mathbf{s}}_2 \cdot \hat{\mathbf{g}}_2 & \hat{\mathbf{s}}_2 \cdot \hat{\mathbf{g}}_3 \\ \hat{\mathbf{s}}_3 \cdot \hat{\mathbf{g}}_1 & \hat{\mathbf{s}}_3 \cdot \hat{\mathbf{g}}_2 & \hat{\mathbf{s}}_3 \cdot \hat{\mathbf{g}}_3 \end{pmatrix} \quad (1)$$

(i.e. $a_{ij} = \hat{\mathbf{s}}_i \cdot \hat{\mathbf{g}}_j$). Here $\hat{\mathbf{s}}_i = (s_{iN}, s_{iE}, s_{iD})$ are unit vectors in the principal stress directions with respect to the geographic coordinate system (\mathbb{G}), and $\hat{\mathbf{g}}_1 = (1, 0, 0)$, $\hat{\mathbf{g}}_2 = (0, 1, 0)$ and $\hat{\mathbf{g}}_3 = (0, 0, 1)$ are the basis vectors in the geographic coordinate system. The normal vector expressed with respect to the principal stress system is then

$$\hat{\mathbf{n}}_{\mathbb{S}} = \mathbf{A}_{\mathbb{S}\mathbb{G}} \hat{\mathbf{n}}_{\mathbb{G}} = \begin{pmatrix} s_{1N}n_N + s_{1E}n_E \\ s_{2N}n_N + s_{2E}n_E \\ s_{3N}n_N + s_{3E}n_E \end{pmatrix}, \quad (2)$$

where, for example, s_{1N} is the north component of the $\hat{\mathbf{s}}_1$ unit vector. In the principal coordinate system, the stress tensor is diagonal

$$\mathbf{S}_{\mathbb{S}} = \begin{pmatrix} S_1 & 0 & 0 \\ 0 & S_2 & 0 \\ 0 & 0 & S_3 \end{pmatrix} \quad (3)$$

and the normal stress acting on the vertical plane of interest is

$$\mathbf{s}_n = (\hat{\mathbf{n}}_{\mathbb{S}}^T \mathbf{S}_{\mathbb{S}} \hat{\mathbf{n}}_{\mathbb{S}}) \hat{\mathbf{n}}_{\mathbb{S}}, \quad (4a)$$

$$= [S_1(s_{1N}n_N + s_{1E}n_E)^2 + S_2(s_{2N}n_N + s_{2E}n_E)^2 + S_3(s_{3N}n_N + s_{3E}n_E)^2] \hat{\mathbf{n}}_{\mathbb{S}} \quad (4b)$$

$$= S_n \hat{\mathbf{n}}_{\mathbb{S}}, \quad (4c)$$

where $S_n = ||\mathbf{s}_n||$. This normal stress corresponds to the horizontal stress in the direction of $\hat{\mathbf{n}}$.

The normal stress expressed by eq. (4b) is quadratic in the plane-normal coordinates, irrespective of the plane's orientation. Eq. (4b) does not describe an ellipse in the horizontal plane (corresponding, for instance, to a horizontal section through the stress ellipsoid) but rather a more complicated figure whose peanut-like shape reflects the dependency on squared sines and cosines. In fact, the normal stress magnitudes of arbitrarily oriented planes define a 3-D peanut shape, illustrated in Fig. 1. We refer to this surface as the 'normal stress surface' and to its profile in the horizontal plane as the 'normal stress section'. The normal stress surface has previously been referred to as the 'Reynolds glyph' in fluid mechanical and geomechanical work (Moore *et al.* 1995, cited by Hashash *et al.* 2003). The normal stress surface is a more convenient representation of the state of stress in this context than the more commonly encountered stress ellipsoid, as the distance from any point on the surface to the origin is equal to the magnitude of the normal stress acting in that direction. This is not true of the stress ellipsoid. In Fig. 1, we illustrate how two stress states, which differ only in terms of their stress ratios, R , yield very different normal stress surfaces, and corresponding normal stress sections.

The different normal stress sections illustrated in Fig. 1 yield different \mathbf{S}_H trends, in spite of the principal stress axes' directions being the same in both cases. We can find the direction of the maximum horizontal stress analytically by differentiating eq. (4b) with respect to α .

$$\frac{dS_n}{d\alpha} = [S_1(s_{1E}^2 - s_{1N}^2) + S_2(s_{2E}^2 - s_{2N}^2) + S_3(s_{3E}^2 - s_{3N}^2)] \sin 2\alpha + 2[S_1s_{1N}s_{1E} + S_2s_{2N}s_{2E} + S_3s_{3N}s_{3E}] \cos 2\alpha. \quad (5)$$

In general (*cf.* Table 2 below), S_n has one maximum and one minimum in the interval $0 \leq \alpha \leq \pi$ and setting the derivative in eq. (5) to zero, we find these stationary points:

$$\tan 2\alpha = \frac{2(S_1s_{1N}s_{1E} + S_2s_{2N}s_{2E} + S_3s_{3N}s_{3E})}{S_1(s_{1N}^2 - s_{1E}^2) + S_2(s_{2N}^2 - s_{2E}^2) + S_3(s_{3N}^2 - s_{3E}^2)}. \quad (6)$$

Using the second derivative of S_n with respect to α we can determine whether $S_n(\alpha)$ yields a maximum or a minimum value, and identify the \mathbf{S}_H trend (α_H) accordingly:

$$\alpha_H = \begin{cases} \alpha & \text{if } S_n(\alpha) \text{ is a maximum} \\ \alpha + \pi/2 & \text{if } S_n(\alpha) \text{ is a minimum.} \end{cases} \quad (7)$$

Fig. 1 illustrates the directions and magnitudes of horizontal normal stress \mathbf{s}_n for the two stress states. For comparison, we also show the direction of the projection of $\hat{\mathbf{s}}_1$ on the horizontal plane, which in this reverse state of stress corresponds to the maximum horizontal stress proxy \mathbf{S}_P . The direction of \mathbf{S}_H calculated using eq. (6) agrees as expected with the direction of maximum normal stress in the horizontal slices whereas \mathbf{S}_H and \mathbf{S}_P become increasingly discrepant as R decreases.

Eq. (6) appears to indicate that we need to know the magnitudes of the stresses to infer the direction of the maximum horizontal

stress. This is not the case, however, as will be demonstrated in the following section.

2.2 Calculating the direction of maximum horizontal stress from focal mechanism stress inversion results

As noted in the introduction, routine stress tensor estimation using earthquake focal mechanism observations does not, in general, retrieve all six independent components of the complete stress tensor. Rather, only the directions of the three principal stresses and a relative measure of the magnitude of the intermediate principal stress, for example, $R = (S_1 - S_2)/(S_1 - S_3)$ (after Etchecopar *et al.* 1981; Gephart & Forsyth 1984), can be estimated. Nevertheless, the four parameters estimated from focal mechanism inversions are sufficient to estimate the direction of the maximum horizontal stress axis, \mathbf{S}_H , but not its magnitude.

In order to estimate the direction of \mathbf{S}_H , we follow the procedure described by Lund (2000) and decompose the stress tensor in the principal stress coordinate system into deviatoric (D) and isotropic ($S_3 \mathbf{I}$) parts.

$$\mathbf{S}_S = (S_1 - S_3) \begin{pmatrix} 1 & 0 & 0 \\ 0 & 1 - R & 0 \\ 0 & 0 & 0 \end{pmatrix} + S_3 \mathbf{I} = \mathbf{D} + S_3 \mathbf{I}. \quad (8)$$

As above, we transform the unit normal of a vertical plane from geographic coordinates ($\hat{\mathbf{n}}_G$) into the principal stress coordinate system, yielding $\hat{\mathbf{n}}_S$. Since we are only interested in the orientation of \mathbf{S}_H we ignore the isotropic part of the stress tensor when calculating the component of normal stress on the vertical plane. By definition, the isotropic part of \mathbf{S} has no directionality and, therefore, does not contribute to the orientation of \mathbf{S}_H . The deviatoric component of normal stress on the vertical plane is

$$\mathbf{d}_n = (\hat{\mathbf{n}}_S^T \mathbf{D} \hat{\mathbf{n}}_S) \hat{\mathbf{n}}_S \quad (9a)$$

$$= (S_1 - S_3) [(s_{1N}n_N + s_{1E}n_E)^2 + (1 - R)(s_{2N}n_N + s_{2E}n_E)^2] \hat{\mathbf{n}}_S \quad (9b)$$

$$= D_n \hat{\mathbf{n}}_S. \quad (9c)$$

This expression for \mathbf{d}_n is also the deviatoric horizontal stress in direction α .

Once again, we find the direction of \mathbf{S}_H by differentiating the magnitude of \mathbf{d}_n with respect to α .

$$\frac{dD_n}{d\alpha} = (S_1 - S_3) [(s_{1E}^2 - s_{1N}^2) + (1 - R)(s_{2E}^2 - s_{2N}^2)] \sin 2\alpha + 2(S_1 - S_3) [s_{1N}s_{1E} + (1 - R)s_{2N}s_{2E}] \cos 2\alpha. \quad (10)$$

Setting the derivative to zero, we find the stationary points at which \mathbf{d}_n has its maximum and minimum magnitudes:

$$\tan 2\alpha = \frac{2(s_{1N}s_{1E} + (1 - R)s_{2N}s_{2E})}{(s_{1N}^2 - s_{1E}^2) + (1 - R)(s_{2N}^2 - s_{2E}^2)}. \quad (11)$$

Table 2. Summary of the conditions under which the denominator of eq. (11) equals zero. α_H and α_1 denote the trends of the axis of maximum horizontal stress, \mathbf{S}_H , and the principal axis of maximum compressive stress, $\hat{\mathbf{s}}_1$, respectively.

Condition	Interpretation
$s_{1N} = \pm s_{1E}$ and $R = 1$	\mathbf{S}_H undefined if $\hat{\mathbf{s}}_1$ vertical, else $\alpha_H = \alpha_1$ (45° or 135°)
$s_{1N} = \pm s_{1E}$ and $s_{2N} = \pm s_{2E}$	\mathbf{S}_H undefined if $R=0$, else $\alpha_H = \alpha_1$ trend (45° or 135°)
$(s_{1N}^2 - s_{1E}^2) + (1 - R)(s_{2N}^2 - s_{2E}^2) = 0$	\mathbf{S}_H undefined if $R=0$, else $\alpha_H = \alpha_1$ trend (45° or 135°)

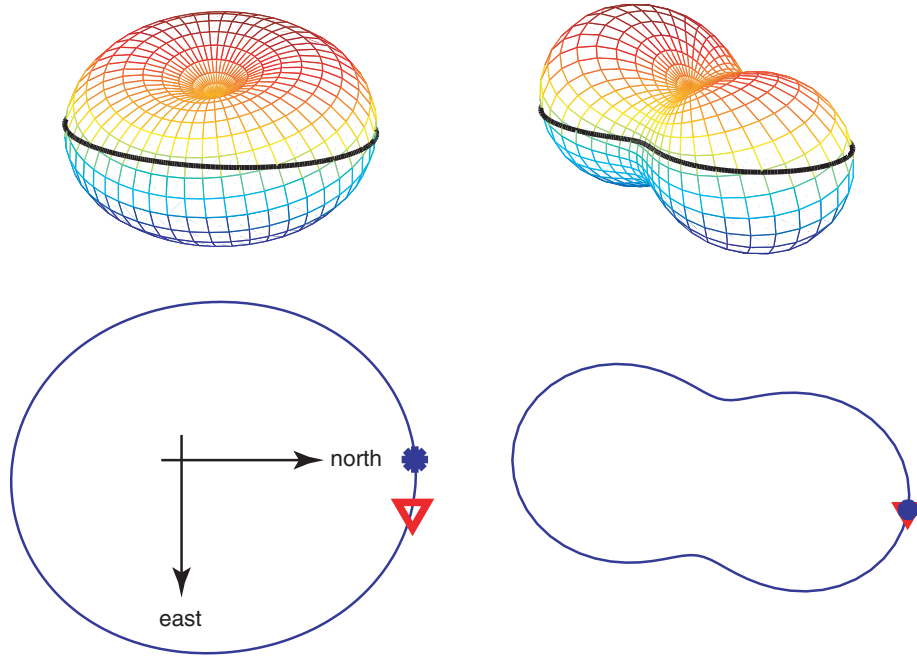


Figure 1. Normal stress surfaces (upper plots) showing the variation in the magnitude of the normal stress acting on surfaces of all orientations. The radius of the normal stress surface in a direction \hat{n} is equal to the magnitude of the normal stress acting in that direction, $S_n = ||s_n||$. The black lines outline the horizontal plane. Horizontal sections (lower plots) through the surfaces show the magnitude of the horizontal (normal) stress: the red and blue symbols mark the trend of \hat{s}_1 and S_H , respectively. The two cases illustrated here have the same principal axis orientations, but different values of the stress ratio $R = (S_1 - S_2)/(S_1 - S_3)$ (after Etchecopar *et al.* 1981; Gephart & Forsyth 1984). The principal stress axes (*trend/plunge*, all angles in degrees) are $\hat{s}_1 = 10/10$, $\hat{s}_2 = 103/17$, $\hat{s}_3 = 251/70$ and $R = 0.1$ and $R = 0.8$ for the left- and right-hand cases, respectively.

The stationary points do not depend on the absolute stress magnitudes, and the minimum principal stress is involved only via R . The direction of S_H , therefore, depends solely on the horizontal components of \hat{s}_1 and \hat{s}_2 and R , as seen from eq. (11). As above, we use the second derivative of D_n with respect to α to determine whether α yields a maximum or a minimum magnitude, and identify the S_H direction accordingly (*cf.* eq. 7). This step requires us to know only the sign of $(S_1 - S_3)$, which is positive in all cases of interest: it cannot be negative, by definition, and if $(S_1 - S_3)$ is zero the stress ellipsoid is a sphere, R is undefined, and so is S_H . Note that since we cannot determine the magnitude of the maximum horizontal stress from the deviatoric stress tensor alone, S_H is in this context a unit vector (although we omit the caret for simplicity, and represent it as S_H rather than \hat{S}_H). Note also that eq. (11) is singular for some stress states, which therefore require special attention (Table 2).

3 CONTROLS ON THE AXIS OF MAXIMUM HORIZONTAL COMPRESSIVE STRESS

In this section, we illustrate the importance of computing a true S_H direction, as opposed to using a proxy (S_P) such as the trend of whichever of \hat{s}_1 and \hat{s}_2 is more horizontal. We start with some idealised examples, in which we consider various permutations of a representative principal stress axis geometry. The reference stress geometry we choose—with axes oriented (*trend/plunge*, in degrees) in the directions 010/10, 103/17 and 251/70—is typical of stress inversion results in that the principal stress directions are slightly off horizontal and vertical. The section ends with examples of focal mechanism stress inversions and comparisons of S_H and S_P using earthquake data from northern Iceland.

3.1 Effects of variations in the stress ratio parameter

The stress ratio R describes the magnitude of the intermediate principal stress S_2 with respect to the maximum and minimum principal stress magnitudes, S_1 and S_3 , as defined in Section 2.2. The value of R , therefore, affects the shape of the stress ellipsoid and the normal stress surface and section, as illustrated by Fig. 1. As R varies from zero to one, S_2 varies from S_1 to S_3 , which causes the stress state to change from one axially symmetric state (corresponding to an oblate stress ellipsoid) via a fully 3-D state to a second axially symmetric state (with a prolate stress ellipsoid; Simpson 1997). In Fig. 2, we show how the direction of S_H varies with the value of R for normal, strike-slip and reverse states of stress. Fig. 2 shows clearly that for normal and reverse stress states, S_H can vary greatly with even small variations in R . This happens when the magnitude of the intermediate stress approaches S_1 and the normal stress surface becomes more spherical and less peanut-like.

3.2 Effects of variations in the stress axes' orientations

The deviations of the principal stress axes from horizontal and vertical directly affect the orientation of S_H . Two stress states with the same principal stress magnitudes but differing in having sub-horizontal and subvertical \hat{s}_1 axes will obviously have different S_H orientations. This is because as \hat{s}_1 becomes more vertical, \hat{s}_2 predominates in the horizontal plane. Fig. 3 illustrates how the S_H trend varies as two of the principal stress axes are rotated about the third, for three related initial stress configurations. We include the effect of variations in R to illustrate the complexity of the relationship between the four seismologically measurable parameters and the S_H axis. For comparison, we also show the trend of the maximum horizontal stress proxy S_P .

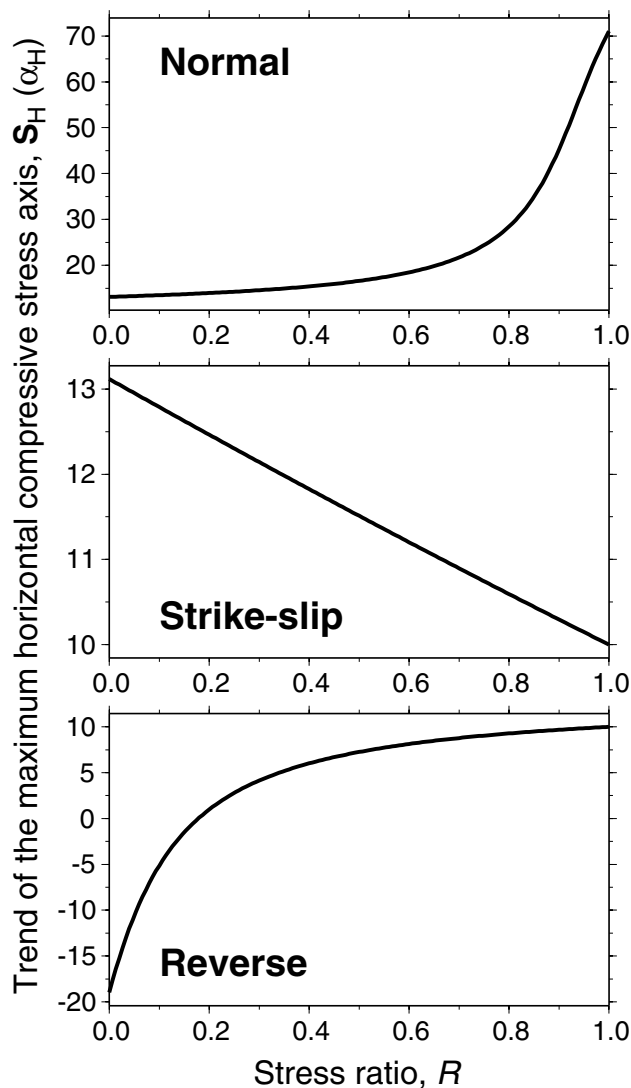


Figure 2. Variation of the S_H trend as a function of the stress ratio R for three different stress axis geometries. The principal stress axes (see Fig. 1 caption) are as follows: upper (normal)— $\hat{s}_1 = 251/70$, $\hat{s}_2 = 10/10$, $\hat{s}_3 = 103/17$; middle (strike-slip)— $\hat{s}_1 = 10/10$, $\hat{s}_2 = 251/70$, $\hat{s}_3 = 283/-17$; and lower (reverse)— $\hat{s}_1 = 10/10$, $\hat{s}_2 = 103/17$, $\hat{s}_3 = 251/70$.

We see from Fig. 3 that variations in the directions of the principal stress axis do indeed affect S_H markedly, and that the effect is rather complicated. For variations in the principal stress axes of up to 90° , we observe variations in S_H of more than 150° . As Fig. 2 reveals, strike-slip stress states exhibit comparatively small variations in S_H direction with R , for fixed stress geometries, and small variations in the principal stress directions do not cause particularly large S_H direction changes either. For reverse and normal-faulting stress states, however, even small changes in the principal stress axes' directions can produce substantial changes in the S_H direction.

3.3 Effects of uncertainties in stress parameter estimates

We are concerned in this paper with the transformation of routinely estimated stress parameters into more straightforwardly viewed and interpreted S_H azimuths, rather than with the methods used to estimate the stress parameters in the first place. Consequently, we do not address here the question of estimating S_H uncertainties (*cf.*

Hardebeck & Hauksson 2001; Townend 2006, and references therein), which stem directly from the estimated uncertainties in the directions of the principal stresses and the stress ratio R . For the purposes of illustration, however, Fig. 4 shows examples of uncertainties in the principal stress directions and R being mapped into a range of S_H trends. Fig. 4 depicts normal strike-slip and reverse stress regimes with moderate departures from idealized Andersonian geometries and representative uncertainties in the principal stress axes' geometries and the stress ratio R . The parameters illustrated here were computed from real focal mechanism data using a recently developed algorithm that incorporates uncertainties in the focal mechanism estimates themselves (Arnold & Townend 2007). Note that we have omitted labels on the probability density contours shown on each stereonet, as these are not readily comparable between different figures. The histograms are presented with vertical scales, although what are key to interpreting these probability density distributions visually are the *relative* positions, heights and widths of the peaks.

As noted above, the difference between the azimuth of maximum horizontal compressive stress and its proxy is most pronounced in normal and reverse cases. In the particular example of a normal stress state illustrated in Fig. 4, the peak in the S_H distribution lies slightly anticlockwise (lower azimuth) of the peak in the S_2 distribution, due to a small contribution in the horizontal plane of a larger but steeply plunging S_1 axis. In the reverse case, the difference between S_H and S_P is minimal (reflecting the fact that the distribution of R is such that S_1 predominates over S_2 in the horizontal plane despite its slight plunge).

3.4 Regional application

To illustrate the effects of the S_H calculation using real data, we present here differences in S_H and S_P directions using focal mechanism stress inversion results from a small section of the Tjörnes fracture zone in northern Iceland (Fig. 5). The Tjörnes fracture zone is an oceanic transform zone in the Mid-Atlantic Ridge system connecting the on-shore North Volcanic Zone in northern Iceland to the off-shore Kolbeinsey Ridge further north (e.g. Saemundsson 1974). Seismicity in the Tjörnes fracture zone defines two main WNW-striking lineaments, the Grímsey lineament and the Húsavík–Flatey fault (Einarsson 1991; Rögnvaldsson *et al.* 1998). The right-lateral Húsavík–Flatey fault is considered the predominant structure in the Tjörnes fracture zone (e.g. Gudmundsson *et al.* 1993; Riedel *et al.* 2005), whereas the Grímsey lineament, where our data come from, is not defined by a continuous fault but rather composed of enechelon structures, namely NNE-striking normal faults and grabens offset by N–S-striking subvertical planes exhibiting left-lateral motion (Rögnvaldsson *et al.* 1998). The overall strike of the Grímsey lineament is $N128^\circ E$ (Rögnvaldsson *et al.* 1998) and comparing this to the plate motion direction of $N103^\circ E$ (DeMets *et al.* 1994), we see that there is a significant component of opening across the Grímsey lineament.

We focus here on stress inversion results from the central portion of the Grímsey lineament, south of the Grímsey hydrothermal field (Riedel *et al.* 2001) and the site of intense seismic activity in recent years. Our data set contains 1653 earthquakes recorded by the Icelandic SIL network (South Iceland Lowland; Bödvarsson *et al.* 1999) between October 2000 and March 2006. Magnitudes range from M_L 0.3 to 4.5. All events have focal mechanisms calculated using the spectral amplitude method of Rögnvaldsson & Slunga (1993) following routine SIL network analysis (Bödvarsson *et al.* 1999). Focal mechanisms of the 20 largest events ($M_L > 3$)

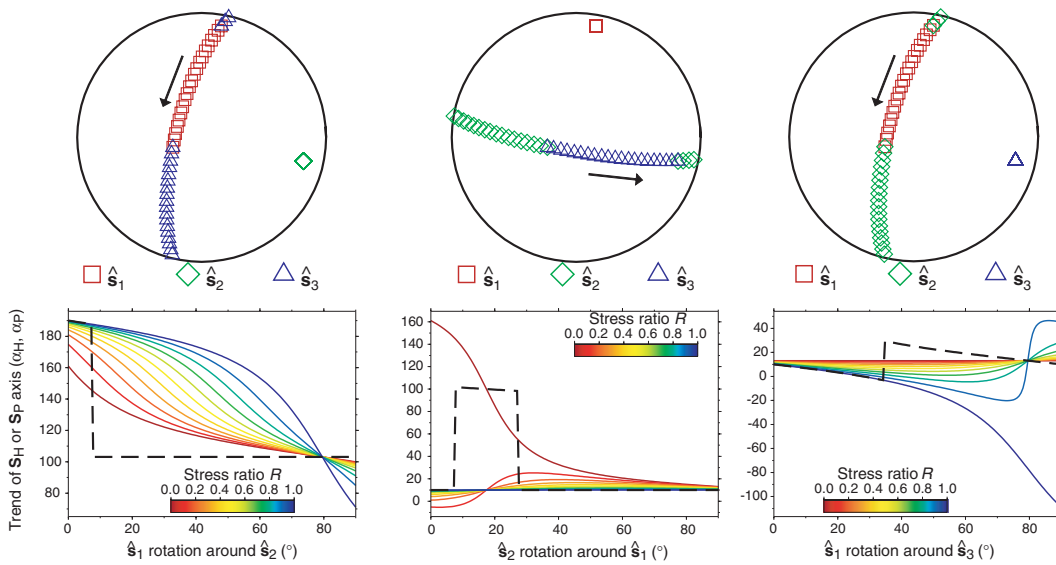


Figure 3. Variation of the S_H and S_P trends (α_H and α_P , respectively) for progressive rotations of the stress axes and different values of the stress ratio R . (Left) Rotation about \hat{s}_2 from a reverse stress state to a normal stress state. (Centre) rotation about \hat{s}_1 from a reverse stress state to a strike-slip stress state. (Right) rotation about \hat{s}_3 from a strike-slip stress state to a normal stress state. The initial geometry is $\hat{s}_1 = 010/10$, $\hat{s}_2 = 103/17$ and $\hat{s}_3 = 251/70$ in the left and centre columns and $\hat{s}_1 = 010/10$, $\hat{s}_2 = 251/70$, and $\hat{s}_3 = 283/-17$ in the right column. The upper plot in each column is a stereographic representation of the different stress states, with north at the top of the circles. The lower plot illustrates the variation in S_H for different values of R (solid coloured curves) as well as the trend of whichever of \hat{s}_1 or \hat{s}_2 is more horizontal (dashed curve).

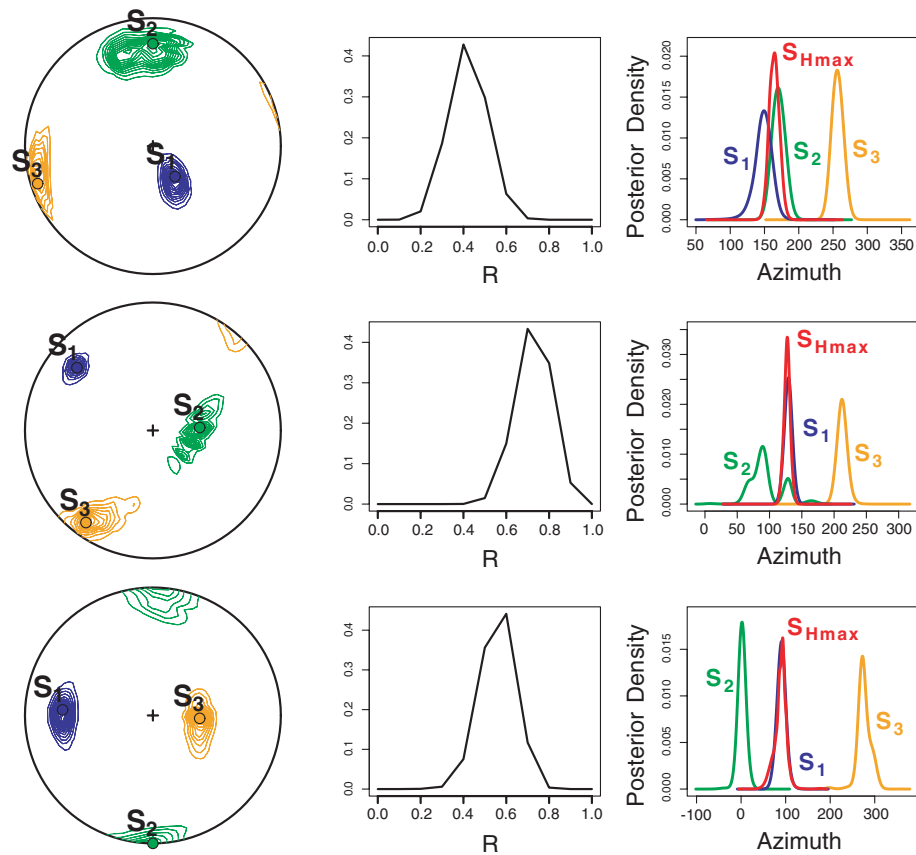


Figure 4. Three examples of uncertainties in stress inversion parameters propagating into uncertainty in S_H for different stress states (see Arnold & Townend 2007, for more details of the algorithm and results). The upper, middle and lower rows correspond to normal, strike-slip and reverse stress states, respectively. The left-hand, middle and right-hand columns contain stereonets illustrating the 3-D distributions of the estimated principal stress axes, histograms showing the uncertainties in the stress ratio R , and histograms of the principal stress axis and S_H trends.

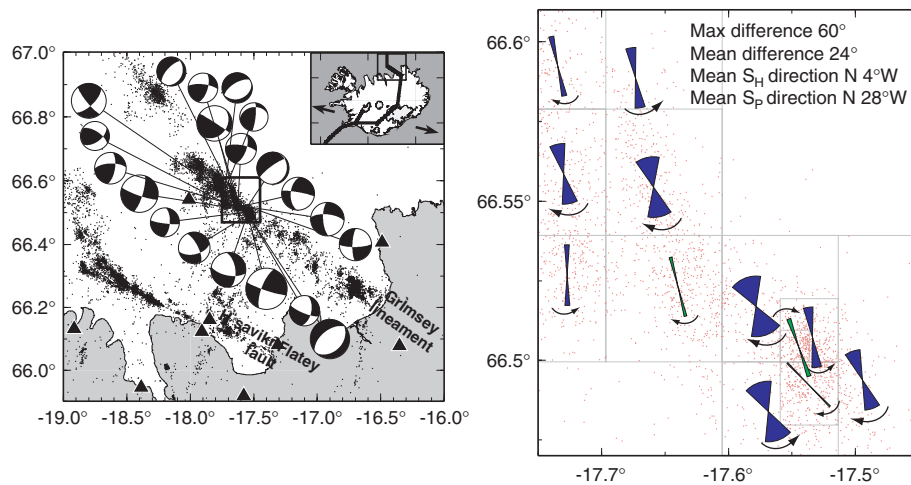


Figure 5. Stress inversion results from northern Iceland demonstrating the difference between S_H and S_P . (Left) Map of the Tjörnes fracture zone, northern Iceland, showing the Grimsey lineament and Húsavík–Flatey fault. The portion of the Grimsey lineament shown in the right-hand figure is illustrated by the box. The focal mechanisms illustrated correspond to the 20 largest ($M_L > 3$) earthquakes occurring within the boxed region between October 2000 and March 2006. The black triangles denote stations in the SIL seismic network. The inset is a map of Iceland showing the outline of the plate boundary and the Tjörnes fracture zone (box), and the North America–Eurasia plate spreading direction (DeMets *et al.* 1994). Note that at these latitudes (66.5°N), 0.1° of longitude corresponds to approximately 4.4 km, and 0.1° of latitude to approximately 11 km. (Right) Angular differences between the trend of the axis of maximum horizontal stress (S_H) calculated using eq. (11) and the trend of the larger subhorizontal principal stress (the maximum horizontal stress proxy, S_P). Blue indicates a normal faulting stress state and green a strike-slip state. Red dots mark the epicentres of earthquakes whose focal mechanisms were used to compute the stress parameters. The arrow symbols indicate the sense of rotation from S_P to S_H . Maximum and mean differences are calculated using the absolute values of the angular differences.

are shown in Fig. 5. These largest mechanisms are predominantly strike-slip but most of the focal mechanisms in our data set exhibit oblique normal to strike-slip faulting, in keeping with the discussion above. The large events are not anomalous as an extensional stress state does not preclude strike-slip faulting on pre-existing structures, although it is less ideal in Andersonian terms than optimally oriented normal faulting. The stress field calculations are based on a recursive ('quadtree') division of the data set into spatially distinct groups containing an average of 160 focal mechanisms each (Townend & Zoback 2001). The number of focal mechanisms in each group is reduced (to an average of 60) using the correlation technique described by Lund & Bödvarsson (2002), which shortens the time required for each inversion and yields more realistic confidence intervals. We calculate the stress orientations and stress ratio for each group using a grid search algorithm that incorporates a fault stability criterion to distinguish the nodal planes (Lund & Slunga 1999).

We have not yet undertaken a detailed analysis of regional stress near the Grimsey lineament, and limit our analysis of the results illustrated in Fig. 5 to a brief comment on how S_H and S_P differ. Most of the stress inversions indicate a normal state of stress (subvertical \hat{s}_1), although a subset of the results are strike-slip (subvertical \hat{s}_2). This agrees with the observations referred to above of a considerable normal-faulting component in the Grimsey lineament. Comparing the S_H directions with the maximum horizontal stress proxy, S_P , reveals some appreciable differences, which in a few cases exceed 30° . The average discrepancy, calculated using the absolute value of the difference in trend between S_H and S_P , is 24° , a non-negligible difference if S_H were to be interpreted accurately in the context of fault mechanics or in conjunction with other geophysical parameters. Note also that for our area of study, using S_P instead of S_H introduces a westerly bias in the estimates, on average. As expected based on the analysis presented in Section 3.2, the discrepancies are generally larger for the normal stress states than the strike-slip.

4 SUMMARY

Calculating a true direction of maximum horizontal compressive stress allows all four seismologically determinable stress parameters to be amalgamated into a single readily visualized and physically meaningful parameter. This simplifies regional stress mapping and the comparison of spatially or temporally distinct stress estimates, procedures which are otherwise complicated by the lack of full knowledge of the stress parameters.

As Figs 1–3 illustrate, the S_H trend is not, in general, equal to the trend of the larger of the two subhorizontal principal stresses (S_P), and in some circumstances may differ by tens of degrees. These differences amount to surmountable errors in interpreting stress inversion results. Correctly accounting for the effects of plunging principal stress axes and variable stress magnitude ratios is paramount in investigating changes in ambient stress caused by either nearby earthquakes or volcanic processes.

It is straightforward to compute a true axis of maximum horizontal compressive stress, and avoid the artefacts introduced by projected plunging stress axes onto a horizontal plane. For reliable comparison of tectonic stress directions with other geophysical parameters—such as horizontal strain rate directions, seismic fast directions or borehole data—we recommend making use of all four seismologically determinable parameters to calculate S_H . The approach we have taken here may also prove useful when mapping other tensorial properties, such as hydraulic conductivity, when the principal axes are not strictly horizontal and vertical. It can also be straightforwardly adapted for use in making vertical cross-sections or maps of arbitrary orientation.

ACKNOWLEDGMENTS

The Icelandic earthquake data were generously provided by the Icelandic Meteorological Office. We thank Richard Arnold for

preparing Fig. 4. We also thank Carole Petit and Mario Mattia for constructive reviews. Python, C and Fortran implementations of eq. (11) as callable functions are available from the first author or at <http://www.geofys.uu.se/bl/SH.html>.

REFERENCES

- Abers, G.A. & Gephart, J.W., 2001. Direct inversion of earthquake first motions for both the stress tensor and focal mechanisms and application to southern California, *J. geophys. Res.*, **106**, 26 523–26 540.
- Anderson, E., 1951. *The Dynamics of Faulting*, 2nd edn, Oliver and Boyd, Edinburgh.
- Angelier, J., 1979. Determination of the mean principal directions of stresses for a given fault population, *Tectonophysics*, **56**, T17–T26.
- Arnold, R. & Townend, J., 2007. A Bayesian approach to estimating tectonic stress from seismological data, *Geophys. J. Int.*, doi: 10.1111/j.1365-246X.2007.03485.x.
- Balfour, N.J., Savage, M.K. & Townend, J., 2005. Stress and crustal anisotropy in Marlborough, New Zealand: evidence for low fault strength and structure-controlled anisotropy, *Geophys. J. Int.*, **163**, 1–14, doi:10.1111/j.1365-246X.2005.02783.x.
- Becker, T., Hardebeck, J. & Anderson, G., 2005. Constraints on fault slip rates of the southern California plate boundary from GPS velocity and stress inversions, *Geophys. J. Int.*, **160**, 634–650, doi:10.1111/j.1365-246X.2004.02528.x.
- Böðvarsson, R., Rögnvaldsson, S.T., Slunga, R. & Kjartansson, E., 1999. The SIL data acquisition system — at present and beyond year 2000, *Phys. Earth planet. Int.*, **113**, 89–101.
- Bohnhoff, M., Grosser, H. & Dresen, G., 2006. Strain partitioning and stress rotation at the North Anatolian fault zone from aftershock focal mechanisms of the 1999 Izmit $M_w = 7.4$ earthquake, *Geophys. J. Int.*, **166**, 373–385, doi:10.1111/j.1365-246X.2006.03027.x.
- Boness, N.L. & Zoback, M.D., 2006a. Mapping stress and structurally controlled crustal shear velocity anisotropy in California, *Geology*, **34**, 825–828, doi:10.1130/G22309.1.
- Boness, N.L. & Zoback, M.D., 2006b. A multiscale study of the mechanisms controlling shear velocity anisotropy in the San Andreas Fault Observatory at Depth, *Geophysics*, **71**, F131–F146.
- DeMets, C., Gordon, R., Argus, D. & Stein, S., 1994. Effect of recent revisions to the geomagnetic reversal time scale on estimates of current plate motions, *Geophys. Res. Lett.*, **21**, 2191–2194.
- Einarsson, P., 1991. Earthquakes and present-day tectonism in Iceland, *Tectonophysics*, **189**, 261–279.
- Etchecopar, A., Vasseur, G. & Daignieres, M., 1981. An inverse problem in microtectonics for the determination of stress tensors from fault striation analysis, *J. Struct. Geol.*, **3**, 51–65.
- Flesch, L.M., Holt, W.E., Haines, A.J. & Shen-Tu, B., 2000. Dynamics of the Pacific–North American plate boundary in the western United States, *Science*, **287**, 834–836.
- Gephart, J.W. & Forsyth, D.W., 1984. An improved method for determining the regional stress tensor using earthquake focal mechanism data: application to the San Fernando earthquake sequence, *J. geophys. Res.*, **89**, 9305–9320.
- Gudmundsson, A., Brynjólfsson, S. & Jonsson, M., 1993. Structural analysis of a transform fault–rift zone junction in North Iceland, *Tectonophysics*, **220**, 205–221.
- Hardebeck, J.L. & Hauksson, E., 2001. Stress orientations obtained from earthquake focal mechanisms: What are appropriate uncertainty estimates?, *Bull. seism. Soc. Am.*, **91**, 250–262.
- Hardebeck, J.L. & Michael, A.J., 2004. Stress orientations at intermediate angles to the San Andreas fault, California, *J. geophys. Res.*, **109**, B11303, doi:10.1029/2004JB003239.
- Hashash, Y.M.A., Yao, J.I.-C. & D.C., W., 2003. Glyph and hyperstreamline representation of stress and strain tensors and material constitutive response, *Int. J. Num. Anal. Met.*, **27**, 603–626, doi:10.1002/nag.288.
- Lund, B., 2000. Crustal stress studies using microearthquakes and boreholes, *PhD thesis*, Uppsala University.
- Lund, B. & Böðvarsson, R., 2002. Correlation of microearthquake body-wave spectral amplitudes, *Bull. seism. Soc. Am.*, **92**, 2419–2433.
- Lund, B. & Slunga, R., 1999. Stress tensor inversion using detailed microearthquake information and stability constraints: application to Ölfus in southwest Iceland, *J. geophys. Res.*, **104**, 14 947–14 964.
- Moore, J.G., Schorn, S.A. & Moore, J., 1995. Methods of classical mechanics applied to turbulence stresses in tip leakage vortex, in *International Gas Turbine and Aeroengine Congress & Exposition*, no. 11, AMSE: Houston, Texas.
- Riedel, C., Schmidt, M., Botz, R. & Theilen, F., 2001. The Grimsey hydrothermal field offshore North Iceland: crustal structure, faulting and related gas venting, *Earth planet. Sci. Lett.*, **193**, 409–421.
- Riedel, C., Tryggvason, A., Dahm, T., Stefansson, R., Böðvarsson, R. & Gudmundsson, G., 2005. The seismic velocity structure north of Iceland from joint inversion of local earthquake data, *J. Seism.*, **9**, 383–404.
- Rögnvaldsson, S.T. & Slunga, R., 1993. Routine fault plane solutions for local networks: a test with synthetic data, *Bull. seism. Soc. Am.*, **83**, 1232–1247.
- Rögnvaldsson, S.T., Gudmundsson, A. & Slunga, R., 1998. Seismotectonic analysis of the Tjörnes Fracture Zone, an active transform fault in north Iceland, *J. geophys. Res.*, **103**, 30 117–30 129.
- Roman, D.C., Moran, S.C., Power, J.A. & Cashman, K.V., 2004. Temporal and spatial variation of local stress fields before and after the 1992 eruptions of Crater Peak vent, Mount Spurr volcano, Alaska, *Bull. seism. Soc. Am.*, **94**, 2366–2379.
- Saemundsson, K., 1974. Evolution of the axial rift zone in Northern Iceland and the Tjörnes fracture zone, *Geol. soc. Am. Bull.*, **85**, 495–504.
- Simpson, R.W., 1997. Quantifying Anderson's fault types, *J. geophys. Res.*, **102**, 17 909–17 919.
- Townend, J., 2006. What do faults feel? Observational constraints on the stress acting on seismogenic faults, in *Earthquakes: Radiated Energy and Physics of Faulting*, Vol. 170, pp. 313–327, eds Abercrombie, R., McGarr, A., Kanamori, H. & Di Toro, G., Geophysical Monograph Series, doi:10.1029/170GM31, AGU, Washington.
- Townend, J. & Zoback, M.D., 2001. Implications of earthquake focal mechanisms for the frictional strength of the San Andreas fault system, in *The Nature and Significance of Fault Zone Weakening*, Vol. 186, pp. 13–21, eds Holdsworth, R.E., Strachan, R.A., MacLoughlin, J. & Knipe, R.J., Geological Society of London Special Publication.
- Townend, J. & Zoback, M.D., 2004. Regional tectonic stress near the San Andreas fault in central and southern California, *Geophys. Res. Lett.*, **31**, L15S11, doi:10.1029/2003GL018918.
- Townend, J. & Zoback, M.D., 2006. Stress, strain, and mountain building in central Japan, *J. geophys. Res.*, **111**, B03411, doi:10.1029/2005JB003759.
- Zoback, M.D. et al., 2003. Determination of stress orientation and magnitude in deep wells, *Int. J. Rock Min. Sci.*, **40**, 1049–1076.